

Phase-gradient gap-plasmon metasurface based blazed grating for real time dispersive imaging

Yuewang Huang, Qiancheng Zhao, Salih K. Kalyoncu, Rasul Torun, Yumeng Lu, Filippo Capolino, and Ozdal Boyraz

Citation: *Applied Physics Letters* **104**, 161106 (2014); doi: 10.1063/1.4872170

View online: <http://dx.doi.org/10.1063/1.4872170>

View Table of Contents: <http://scitation.aip.org/content/aip/journal/apl/104/16?ver=pdfcov>

Published by the [AIP Publishing](#)

Articles you may be interested in

[Impact of spectral broadening on plasmonic enhancement with metallic gratings](#)

Appl. Phys. Lett. **101**, 121102 (2012); 10.1063/1.4753806

[Trapping of surface plasmon waves in graded grating waveguide system](#)

Appl. Phys. Lett. **101**, 013111 (2012); 10.1063/1.4733477

[Four-mode plasmonic structure based on a prism-grating anticrossing bandgap](#)

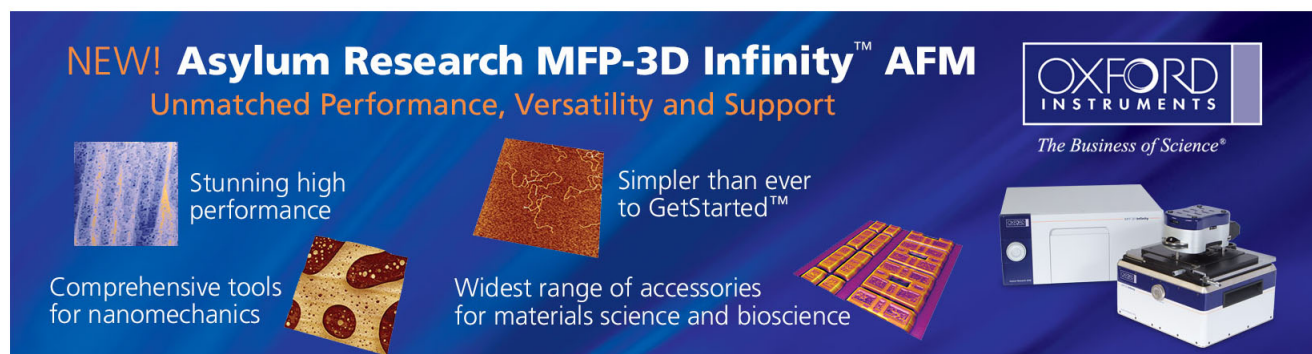
Appl. Phys. Lett. **100**, 063301 (2012); 10.1063/1.3682081

[Study of plasmonic crystals using Fourier-plane images obtained with plasmon tomography far-field superlenses](#)

J. Appl. Phys. **110**, 083109 (2011); 10.1063/1.3654001

[Light Intensity Profile Control along the Optical Axis with Complex Pupils Implemented onto a PhaseOnly SLM](#)

AIP Conf. Proc. **992**, 152 (2008); 10.1063/1.2926847



NEW! Asylum Research MFP-3D Infinity™ AFM
Unmatched Performance, Versatility and Support

OXFORD INSTRUMENTS
The Business of Science®

Stunning high performance
Simpler than ever to GetStarted™
Comprehensive tools for nanomechanics
Widest range of accessories for materials science and bioscience

The advertisement features four images: a blue textured surface, a brown textured surface, a grid of colorful rectangular samples, and the Asylum Research MFP-3D Infinity AFM instrument.

Phase-gradient gap-plasmon metasurface based blazed grating for real time dispersive imaging

Yuewang Huang, Qiancheng Zhao, Salih K. Kalyoncu, Rasul Torun, Yumeng Lu, Filippo Capolino, and Ozdal Boyraz^{a)}

EECS Department, University of California, Irvine, California 92697, USA

(Received 4 February 2014; accepted 10 April 2014; published online 21 April 2014)

Dispersive Fourier transform imaging is a powerful technique in achieving ultrafast imaging of wide areas. However, system power efficiency is often limited by dispersive components. Here, we demonstrate that a gap-plasmon metasurface (GPM) based blazed grating can be used in dispersive imaging applications to achieve higher power efficiency than conventional gratings. A sub-wavelength GPM-based grating at telecommunication wavelengths has been designed and fabricated. 75.6% power efficiency with $\sim 0.4^\circ/10$ nm spatial dispersion has been measured for TE polarized waves at normal incidence. The fabricated device has been tested in a wide area real-time dispersive imaging system and <300 μm spatial resolution has been demonstrated experimentally.

© 2014 AIP Publishing LLC. [<http://dx.doi.org/10.1063/1.4872170>]

Optical signal processing using time wavelength mapping and space wavelength mapping are powerful techniques that can overcome speed and bandwidth limitations of conventional approaches pertinent to digitization, waveform generation, and imaging.¹⁻⁷ In dispersive imaging system, wavelength-to-space mapping was usually realized by using spatially dispersive components, such as diffraction grating, digital micro-mirror devices (DMDs), acoustic-optical deflectors, and virtually imaged phased array.^{2-5,8,9} However, low diffraction or power efficiency associated with these devices often poses serious limitations on the performance of the dispersive imaging systems. Alternative mechanisms have to be sought. Metasurfaces have been recently investigated as a means of sub-wavelength phase manipulation for micro/nano-scale light control.¹⁰⁻¹³ Among all types of proposed metasurfaces, metal-backed metasurface, known as gap-plasmon metasurface (GPM), have the advantage of high efficiency and conservation of polarization.¹⁴⁻¹⁶ A wide range of functional devices based on gap-plasmon metasurface have been proposed or demonstrated recently, including surface wave coupler,¹⁵ polarization splitter,¹⁶ blazed grating,¹⁷ wave plates,¹⁸ focusing mirror,¹⁹ and hologram recording.²⁰

In this paper, the idea of wavefront manipulating plasmonic metasurfaces has been investigated to improve the power efficiency and diffraction efficiency of conventional diffractive optical components. We designed and fabricated a GPM-based blazed grating operating at 1550 nm optical communication band to replace the grating in the dispersive imaging system to improve power efficiency. The fabricated GPM grating consists of an array of unit cells and provides reflection at an angle of $\sim 51^\circ$ with an angular dispersion of $\sim 0.4^\circ/10$ nm. The power efficiency of the grating was measured to be as high as 75.6%. By incorporating the GPM-based grating into the dispersive imaging system, we achieved an imaging resolution of <300 μm . Sub-wavelength manipulation of wave-front phase at infrared

wavelength opens the door to a wide range of telecommunication applications and can be extended to any device based on wavefront engineering.²¹ Since the proposed device is planar, it can be easily integrated with other components, which is a key to future miniaturization of complex systems.

The emerging metasurface is a two-dimensional nano-patterned metallic surface with sub-wavelength features and the wavefront manipulating capability originates from plasmonic resonance in the metallic structures.^{22,23} Each metasurface element acts as an electric dipole scattering with a phase delay controlled by its dimension. Single layer metasurfaces limit the wavefront manipulation to π due to the single dipole nature of the resonance.²² By inserting a ground plane under patterned metasurfaces to form the metal-insulator-metal (MIM) structure, coupling between top metasurface and the ground plane can excite additional dipole oscillation and phase variation up to 2π can be potentially achieved.^{15,17} Higher power efficiency is also expected from high reflection by the ground plane. The inset of Fig. 1(a) shows the stack of the designed GPM unit cell. Silver (Ag) ground plane and Ag top layer are spaced by SiO_2 . In this work, silver and SiO_2 are chosen as the metal and dielectric due to the transparency of SiO_2 and the fact that Ag has four times lower damping compared to gold in the telecommunication window.^{24,25} The proper choice of the dimensions in the unit cell will excite gap surface plasmonic resonance in the MIM structure. The phase of the reflected field is sensitive to the dimensions that are used for small detuning. Fig. 1(a) shows the phase of the reflectivity of the inset GPM unit cell under normal incidence with electrical field polarized along the y direction. A wide range of reflectivity phase can be achieved by tuning the length of the Ag patches. The thickness of the dielectric spacer plays a critical role in determine the tuning range. A thin oxide spacer with a 50 nm thickness is capable of delivering nearly 2π reflectivity phase variation, which is theoretically adequate to generate an arbitrary wavefront profile. Fig. 1(b) illustrates the conceptual design of the GPM-based blazed grating to enable angled reflection. Ten sub-cells grouped by two cells with different

^{a)}E-mail: oboyraz@uci.edu

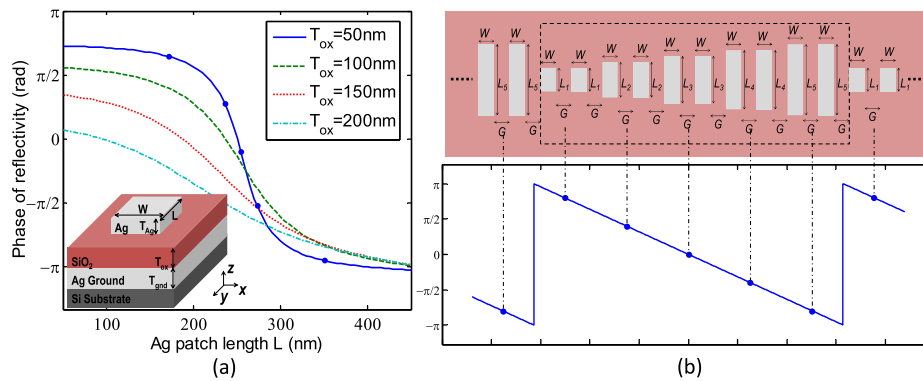


FIG. 1. (a) Phase of reflectivity for GPM unit cell with different geometrical parameters. A phase variation of nearly 2π is achievable when the oxide spacer is 50 nm thick and the tuning range decrease when the oxide thickness increases. (Inset) Stack of a GPM unit cell. The thickness of the ground plane Ag, oxide spacer, and top Ag layer are 200 nm, 50 nm, and 30 nm, respectively. The size of the unit cell is $200 \text{ nm} \times 500 \text{ nm}$. (b) Schematics of the designed sub-wavelength GPM-based blazed grating. Dashed line enclosed a super-cell.

Ag patch lengths are combined to form a super-cell spanning over a phase variation of 2π in a linear fashion (i.e., constant phase gradient). Here, the customized design parameters for a specific application require the optimization of W , L_i , G as well as the number of cells and oxide thickness. For our imaging application, we optimize the GPM-based grating for power efficiency and determine the lengths as $L_1 = 171 \text{ nm}$, $L_2 = 236 \text{ nm}$, $L_3 = 254 \text{ nm}$, $L_4 = 273 \text{ nm}$, and $L_5 = 350 \text{ nm}$, respectively, for the sub-cells, as marked by dots in Fig. 1(a). The width of the top Ag patches is $W = 160 \text{ nm}$ and the space between two patches is $G = 40 \text{ nm}$. The oxide spacer thickness is chosen to be $T_{\text{ox}} = 50 \text{ nm}$. The thickness of the ground plane Ag and top device Ag are selected to be $T_{\text{gnd}} = 200 \text{ nm}$ and $T_{\text{Ag}} = 30 \text{ nm}$, respectively. The super-cell is repeated in both x and y directions periodically to form an in-plane reflection in our design. Out-of-plane extraordinary reflection can also be achieved by offsetting the super-cells along the y direction.¹² The structure repeats itself for every period $\Lambda = 2 \mu\text{m}$ and this gives a phase gradient of $(\nabla\phi)_x = 2\pi/\Lambda$ along the x direction. If the incidence is normal, the reflected wave will have a tangential wave vector component of $k_x = (\nabla\phi)_x$. Hence, the reflected wave will be deflected to an angle according to $k_0 \sin\theta_r = k_x$. For the designed wavelength of $1.55 \mu\text{m}$, this gives a reflected angle of $\theta_r = \sin^{-1}(k_x/k_0) = 50.8^\circ$.

A full wave simulation based on the finite element method (COMSOL) is used to verify the analytical design parameters and estimate the field pattern. Fig. 2 shows the full wave simulation results for the fabricated device. TE

polarized beam incidents from the right and gets deflected to the top. Fig. 2(a) shows the interference pattern of the incident field and reflected field, showing a reflection angle of $\sim 51^\circ$. This agrees very well with the analytically calculated value of 50.8° . Fig. 2(b) shows the phase of only the reflected field and the blazed grating indeed manipulates the wavefront of the incident beam in a nearly linear fashion. Fig. 2(c) shows the phase of scattered wave along the black line and it resembles the desired phase profile in Fig. 1(b). To quantize the device performance, we also calculated the far-field pattern of the scattered wave for three different wavelengths. As shown in Fig. 2(d), most of energy from the incident beam was deflected to an angle of $\sim 49^\circ$, 51° , and 53° , respectively, for 1500 nm, 1550 nm, and 1600 nm. The beam is also well collimated and the FWHM angular width is only 3° . Due to the suppression of higher orders in the sub-wavelength grating, a very high power efficiency of 81.3% was predicted by the far-field radiation pattern at $1.55 \mu\text{m}$ wavelength. When the operating wavelength deviates from the designed wavelength, the power efficiency drops to 73.0% and 79.7% for 1500 nm and 1600 nm, respectively. It is also noteworthy that the far field radiation at around -51° is due to the reflection caused by non-ideal boundary condition in the numerical simulation and therefore artificial.

The device fabrication started with a prime silicon substrate. The 200 nm ground plane Ag was first deposited using E-beam evaporation. To increase adhesion, 5 nm of Cr was deposited on the Si substrate prior to Ag deposition. A

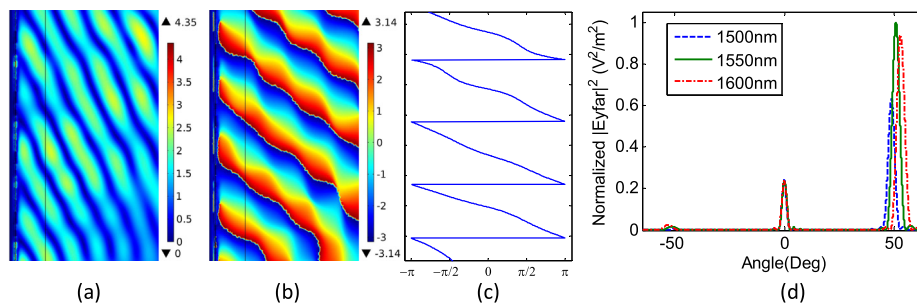


FIG. 2. Full-wave simulation of the designed GPM-based blazed grating: (a) Electrical field distribution showing the interference pattern between the reflected wave and incident wave; (b) Phase distribution of the only reflected field showing that the normal incident is deflected to the top with an angle; (c) The phase of deflected field along the black sampling line in (b) showing that a nearly linear phase profile is generated as expected. (d) Far-field radiation pattern of the scattered wave for different wavelengths.

dielectric spacer layer of 50 nm SiO₂ was then deposited using the same method. We then coated two layers of poly-methyl methacrylate (PMMA) resist (495A4 followed by 950A2) on the processed substrate. Double layer PMMA was used to ease the following lift-off process. Then, we deposited another layer of 30 nm Ag after a 3 nm Cr adhesive layer as before. Since the thickness of the added adhesive layer is much smaller than the skin depth of the metal at the operating frequency, there will be negligible effect on the simulation result as also verified by a careful simulation matching the real device. Finally, lift-off process using acetone was employed to finally define the top Ag pattern. It is noteworthy that the repetitive nature of the device pattern makes it possible to be fabricated with nano-imprinting techniques, which is more economic than E-beam lithography for full wafer scale devices. A SEM image of the fabricated GPM-based grating is shown in Fig. 3(a). The functionality of the fabricated device is tested using a tunable laser. Fig. 3(b) shows the measured deflected angle with respect to wavelength, which is in good agreement with the simulated results. Due to the limitation in angular resolution and wavelength tuning range, only five different wavelengths were measured. Fig. 3(c) shows the deflected angle for different incident angles at the wavelength of 1.55 μm. The reflected angle is quite different from the incident angle, clearly revealing the phenomenon of anomalous reflection.^{10,17} Due to an experimental setup limitation, we only have measurement result for incident angle up to ~8°. As incident angle increases, the power efficiency drops. Simulations show that reflection vanishes when the incident angle is greater than 12°. This can be explained as follows. In the case of oblique incidence with angle θ_i , the incident phase gradient is $k_x^i = k_0 \sin \theta_i$. When we include the phase gradient of $(\nabla\phi)_x = \frac{2\pi}{\Lambda}$ from the metasurface, the propagation constant for the reflected wave along the x direction becomes $k_x^r = \frac{2\pi}{\Lambda} + k_0 \sin \theta_i$. When $k_x^r > k_0$, no reflection will be supported. For a wavelength of 1.55 μm, this gives a critical angle of $\theta_c = 13^\circ$ at which $k_x^r = k_0$. In fact, the incident wave can couple to the surface plasmonic wave after the critical angle.¹⁵ The measured and simulated results show very good agreement and we accounted the slight smaller angle in the measurement to be a systematic error in the experiment setup and/or fabrication, inaccurate electromagnetic constants of materials in simulation, and the aging of top Ag layer. The measured power efficiency for TE-polarized light at 1.55 μm is ~75.6%. This also agrees well with the estimated efficiency of 81.3%.

Recently, we showed fast dispersive laser imaging system utilizing MEMS based DMD and fiber-based dispersion unit.⁵ In this approach, short pulses are first dispersed in time

domain by using chromatic dispersion of optical fibers, and hence each color is displaced in time domain in a serial fashion. Then, temporally displaced colors are assigned to different locations by using a diffraction grating to capture the line image of assigned locations in a serial fashion. While lateral scanning is achieved mechanically by using the DMD, the scanning in the horizontal direction is achieved by the spatial dispersion of the diffraction grating. Due to the intrinsic low efficiency of the DMD arrays, the power efficiency of the entire system is also low and becomes one of the limiting factors of the overall system performance. To alleviate this, the power budget of the every component should be evaluated carefully. In this work, the diffraction grating in the old setup⁵ is replaced by the fabricated GPM-based grating for improved power efficiency.

The experimental setup is shown in Fig. 4(a). First, ultra-short laser pulses are amplified by an Erbium-doped fiber amplifier (EDFA) and then pass through a cascaded fiber optics system consisting of a single-mode fiber (SMF), a dispersion-shifted fiber (DSF), and a highly nonlinear fiber (HNLF) in tandem to generate broadband supercontinuum (SC) source. Then, we use a coarse wavelength division multiplexing (CWDM) filter to carve out ~20 nm bandwidth centered at 1590 nm. These band-limited SC pulses are then fed through the amplified dispersive Fourier transform (ADFT) system, as illustrated by the pulses at the input and output of the ADFT system with different spectral distributions in the blue dotted-line box in Fig. 4(a). The ADFT system accomplishes two goals: wavelength-to-time mapping and power amplification. Wavelength-to-time mapping is achieved through the chromatic dispersion process by using the dispersion compensation module (DCM), hence the name dispersive Fourier transform. Since the DCM has a positive dispersion of $D = 675$ ps/nm, chromatic dispersion maps the shorter wavelengths to the leading edge (earlier in time) and longer wavelengths to the trailing edge (later in time) of the pulse. Meanwhile, the pulses are also expanded to ~13 ns for effective temporal detection using a single-pixel photodiode. Power amplification is achieved by a Raman amplifier using four pump lasers at wavelengths of 1450 nm, 1470 nm, 1490 nm, and 1505 nm in a bi-directional pumping configuration. These time-mapped pulses are then collimated and launched onto a DMD with 1024 × 768 pixel mirror arrays. The micro-mirrors in the DMD are turned to ON state row by row to facilitate vertical scanning. Vertically separated laser beams are then reflected by the GPM-based blazed grating device and different wavelength components are dispersed in the horizontal direction to sample different locations in the target area (wavelength-to-space mapping process). Since different wavelengths are already mapped onto different time

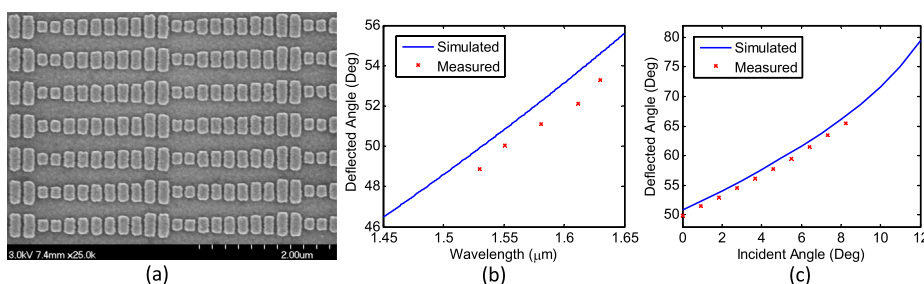


FIG. 3. (a) SEM image of the fabricated device; (b) simulated and measured deflected angle for different wavelengths at normal incidence. (c) Simulated and measured deflected angle for different incident angles at 1.55 μm.

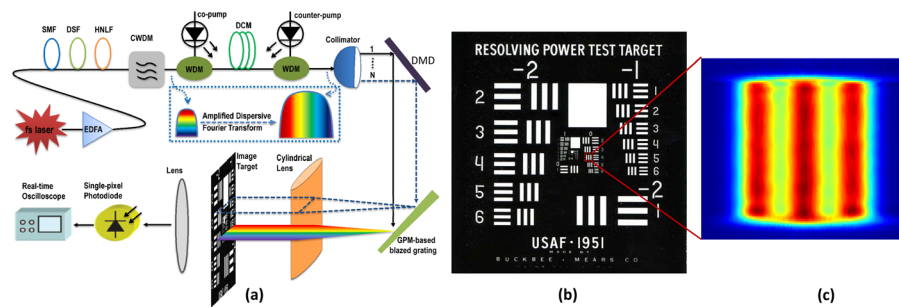


FIG. 4. (a) The setup of the imaging system using the fabricated GPM-based blazed grating. Pulses in blue dotted-line box illustrate the ADFT process, in which different spectral colors are separated in time domain and the pulses are broadened and amplified. SMF: single-mode fiber, DSF: dispersion-shifted fiber, HNLf: highly nonlinear fiber, DCM: dispersion compensation module, DMD: digital micro-mirror device. (b) The whole pattern of 1951 USAF test chart. (c) The recovered image of the area enclosed by the red dashed box in (b) (Element 4 of Group 0 in 1951 USAF). A resolution $<300\ \mu\text{m}$ can be achieved.

instants by the aforementioned ADFT system, information of different locations will be encoded onto different time instants of the pulse, and a space-to-time mapping relationship is essentially established. As a result, we can detect the temporal shape of the optical pulse using a single photodetector and use the detected time domain signal to reconstruct the spatial information of the target at the focal plane. By combining consecutive pulses from different vertical scanning lines, we can capture a 2D image of the target. In this study, we use 1951 USAF test chart, Fig. 4(b), to characterize the imaging resolution. Fig. 4(c) illustrates the recovered image of Element 4 in Group 0 of the test chart (i.e., region enclosed in the red dashed line box in Fig. 4(b)). The vertical lines width and spacing are $354.6\ \mu\text{m}$. We can resolve lines $<300\ \mu\text{m}$ by using this imaging system. Wider area and/or higher resolution can be achieved if a GPM-based grating with a larger fingerprint is available. Compared to our previous approach that uses conventional diffraction gratings, the GPM-based grating provides improvement on system power efficiency. Additionally, plasmonic metasurfaces can be potentially devised to combine different functionalities of multiple devices, e.g., grating and cylindrical lenses, on a single surface and hence further improve the efficiency.^{20,26}

In summary, we present the design, fabrication, and characterization of a planar sub-wavelength blazed grating based on phase-gradient gap-plasmon metasurface in a stacked MIM structure. The size of the Ag patches on the top layer was designed to generate a deflected phase profile with linear gradient along the x -direction. The device was fabricated using E-beam lithography. Measurement results showed that the GPM-based blazed grating reflected normal incident light to an angle of 51° with a FWHM of 3° . The measured power efficiency of 75.6% is much higher than conventional gratings. The fabricated device was then integrated into a fiber-based dispersive imaging system, and we demonstrate imaging with $<300\ \mu\text{m}$ resolution without system optimizing.

This research was partially supported by the National Science Foundation (NSF) Award No. ECCS-1028727. The author would like to thank Shulin Sun from National Taiwan University for valuable discussion.

- ¹J. Chou, O. Boyraz, D. Solli, and B. Jalali, *Appl. Phys. Lett.* **91**, 161105 (2007).
- ²K. Goda, K. K. Tsia, and B. Jalali, *Appl. Phys. Lett.* **93**, 131109 (2008).
- ³F. Qian, Q. Song, E. Tien, S. K. Kalyoncu, and O. Boyraz, *Opt. Commun.* **282**, 4672 (2009).
- ⁴K. Goda, A. Mahjoubfar, C. Wang, A. Fard, J. Adam, D. R. Gossett, A. Ayazi, E. Sollier, O. Malik, E. Chen, Y. Liu, R. Brown, N. Sarkhosh, D. Di Carlo, and B. Jalali, *Sci. Rep.* **2**, 445 (2012).
- ⁵S. K. Kalyoncu, Y. Huang, R. Torun, Q. Zhao, and O. Boyraz, in *Conference on Lasers and Electro-Optics (CLEO)* (Optical Society of America, 2013), p. JTu4A.30.
- ⁶S. K. Kalyoncu, Y. Huang, Q. Song, and O. Boyraz, *IEEE Photonics J.* **5**, 5500207 (2013).
- ⁷K. Goda and B. Jalali, *Nat. Photonics* **7**, 102 (2013).
- ⁸G. D. Reddy and P. Saggau, *J. Biomed. Opt.* **10**, 064038 (2005).
- ⁹P. Metz, J. Adam, M. Gerken, and B. Jalali, *Appl. Opt.* **53**, 376 (2014).
- ¹⁰N. Yu, P. Genevet, M. A. Kats, F. Aieta, J.-P. Tetienne, F. Capasso, and Z. Gaburro, *Science* **334**, 333 (2011).
- ¹¹X. Ni, N. K. Emani, A. V. Kildishev, A. Boltasseva, and V. M. Shalaev, *Science* **335**, 427 (2012).
- ¹²F. Aieta, P. Genevet, N. Yu, M. A. Kats, Z. Gaburro, and F. Capasso, *Nano Lett.* **12**, 1702 (2012).
- ¹³A. V. Kildishev, A. Boltasseva, and V. M. Shalaev, *Science* **339**, 1232009 (2013).
- ¹⁴J. Hao, Q. Ren, Z. An, X. Huang, Z. Chen, M. Qiu, and L. Zhou, *Phys. Rev. A* **80**, 023807 (2009).
- ¹⁵S. Sun, Q. He, S. Xiao, Q. Xu, X. Li, and L. Zhou, *Nature Mater.* **11**, 426 (2012).
- ¹⁶A. Pors, O. Albrektsen, I. P. Radko, and S. I. Bozhevolnyi, *Sci. Rep.* **3**, 2155 (2013).
- ¹⁷S. Sun, K.-Y. Yang, C.-M. Wang, T.-K. Juan, W. T. Chen, C. Y. Liao, Q. He, S. Xiao, W.-T. Kung, G.-Y. Guo, L. Zhou, and D. P. Tsai, *Nano Lett.* **12**, 6223 (2012).
- ¹⁸A. Pors, M. G. Nielsen, and S. I. Bozhevolnyi, *Opt. Lett.* **38**, 513 (2013).
- ¹⁹A. Pors, M. G. Nielsen, R. L. Eriksen, and S. I. Bozhevolnyi, *Nano Lett.* **13**, 829 (2013).
- ²⁰W. T. Chen, K.-Y. Yang, C.-M. Wang, Y.-W. Huang, G. Sun, I.-D. Chiang, C. Y. Liao, W.-L. Hsu, H. T. Lin, S. Sun, L. Zhou, A. Q. Liu, and D. P. Tsai, *Nano Lett.* **14**, 225 (2014).
- ²¹N. Yu, P. Genevet, F. Aieta, M. A. Kats, R. Blanchard, G. Aoust, J.-P. Tetienne, Z. Gaburro, and F. Capasso, *IEEE J. Sel. Top. Quantum Electron.* **19**, 4700423 (2013).
- ²²R. Blanchard, G. Aoust, P. Genevet, N. Yu, M. A. Kats, Z. Gaburro, and F. Capasso, *Phys. Rev. B* **85**, 155457 (2012).
- ²³A. Pors and S. I. Bozhevolnyi, *Opt. Express* **21**, 27438 (2013).
- ²⁴P. B. Johnson and R. W. Christy, *Phys. Rev. B* **6**, 4370 (1972).
- ²⁵P. R. West, S. Ishii, G. V. Naik, N. K. Emani, V. M. Shalaev, and A. Boltasseva, *Laser Photonics Rev.* **4**, 795 (2010).
- ²⁶M. Veysi, C. Guclu, O. Boyraz, and F. Capolino, in *IEEE International Symposium on Antennas and Propagation* (IEEE, Memphis, Tennessee, USA, 2014).